Hypersonic Nonequilibrium Flow Simulation Based on Kinetic Models

J.S. Shang[1], S.T. Surzhikov[2], H. Yan[3]

Wright State University, USA; Russian Academy of Science, Moscow, Russia

Northwestern Polytechnical University, China

[1]joseph.shang@wright.edu; [2]surg@ipmnet.ru; [3]yanhong@nwpu.edu.cn

Abstract

The nonequilibrium hypersonic flowfield over a blunt body is computationally simulated by self-consistent kinetic models. The conservation governing equation is based on the continuum formulation by the kinetic theory of a diluted gas for transport properties, and a group of chemical-physical kinetic models of chemical kinetics for nonequilibrium chemical reactions, and energy transfer among internal degrees of excitation. In this regard, the present analysis summarizes the current progress illuminating efforts for an interdisciplinary computational fluid dynamics endeavour. Further progress of this computational simulation discipline has to be built on the newly found knowledge base.

Keywords

Interdisciplinary CFD; Nonequilibrium Hypersonic Flow

Introduction

Nonequilibrium thermodynamic state and chemical reactions are common features of hypersonic flows. The flow field around a typical blunt body at an altitude above 60 km with a flight speed exceeding 2 km/s cannot maintain a chemical equilibrium state. In the framework of continuum mechanics, the bridge linking the Boltzmann equation and conservative laws of aerodynamics is the kinetic theory of gases through the Chapman-Enskog expansion [1]. Since the kinetic theory does not consider the internal structure of atoms and molecules, the higher degrees of excitation beyond translational motion must be resolved by modelling.

Traditionally the connection between molecular and atomic structures and thermodynamic behaviour of high-temperature gas is described by statistical thermodynamics and augmented by quantum physics. Therefore, the internal degrees of freedom of atomic and molecular species were studied via the partition function and the gas mixture was assumed to be in local equilibrium [2]. A substantial amount of research results have been derived from this approach [3] and more recently even extended to include the ablation phenomenon [4]. However, significant discrepancy has been noted for this group of results when compared with a limited amount of flight data. A part of the discrepancy is due to inaccurate computations and experimental measurements, but a major portion of this disparity is incurred by the modelling of the physics [5-7].

At the present, a thorough understanding of the extremely complex physical-chemical phenomena of nonequilibrium hypersonic flows is still beyond our reach. All the interactions of the internal degrees of freedom occur at the molecular and atomic scales, therefore must be modelled and can be verified only by a sparse validating data base for physical fidelity. For this reason, the present investigation is focused on the blunt-body problem which is dominated by the strong bow shock. In this flowfield the energy content in the translational mode is initially much greater than the vibrational mode which mostly occupies mostly the first few quanta above the ground state. Therefore the classic theory of Landau-Teller provides a creditable approximation [8]. Meanwhile, a separate treatment for nonequilibrium rotational degrees of freedom of gas component may not be necessary. In fact, the rotational excitation can reach its classic equilibrium state by about 10 kinematic collisions to elevate its energy level by one κT. Therefore, it is fully justified to assume the rotational excitation to be in equilibrium with the translational mode [6].

On the other hand, the vibrational relaxation of air becomes significant in the temperature range above 1,000 K and beyond that the molecule dissociated into atoms. At the lower limit of the temperature range, it

is estimated that the vibrational excitation requires from 1,000 to 10,000 collisions to reach thermal equilibrium with the translational mode [6]. Under this circumstance, the energy exchange between different molecular species has a higher probability than the vibration-translation transfer of same molecule [6,7]. In addition, the adiabatic collision has a low probability of vibrational excitation and will not be taken into consideration.

For the electronic excitations, the vibrational energy of the molecule plays a main role in the dissociation. This process will be carefully examined using a detailed analysis for the generation and depletion balance. Finally when the energy of the excitation is greater than 10 eV, the cross sections of inelastic collisions of heavy particles are several orders of magnitude smaller than the cross sections of elastic electron impact [2,3,6]. Therefore, the modelling of ionization by electrons impact will be emphasized.

All the accumulative knowledge in treating the detailed physical-chemistry modelling has guided the development of the widely used model equations for nonequlibrium hypersonic flow simulations [3-12]. It would be valuable to summarize the current state-of – the-art in kinetic modelling and to project future basic research needs for better understanding.

Governing Equation

By examining the governing equations in the continuum domain, the effects of internal atomic and molecular structures are explicitly contained in the species and energy conservation equations, but only implicitly in the conservation law of momentum through the transport property of the gas mixture. The coupling of conservation laws has offered a wide range of options on how this interdisciplinary equation system can be efficiently solved. On the other hand, the quantum levels of rotational excitation are densely packed and readily reach equilibrium with translational excitation, but this fundamental mode is not necessarily equilibrated with the vibrational and electronic excitations [2]. In the present approach, the energy exchange/cascade between vibration-translation and electronic-translation interactions will be explicit simulated by the separated energy conservation equations for vibrational and electronic excitations [7]. In other words, the present approach is built on a refined energy balance from the internal structure of the atom and molecule. The detailed mechanisms are developed by models of the gas kinetics. The conservation equations in a continuum medium can be given as [5,7];

$$\frac{\partial \rho_i}{\partial t} + \nabla \cdot [\rho_i (\vec{u} + \vec{u}_i)] = \frac{dw_i}{dt} \tag{2-1}$$

$$\frac{\partial \rho \vec{u}}{\partial t} + \nabla \cdot (\rho \vec{u}\vec{u} + p\vec{\vec{I}} - \vec{\vec{\tau}}) = 0 \tag{2-2}$$

$$\frac{\partial \rho e}{\partial t} + \nabla \cdot [\rho e \vec{u} - \kappa \nabla T + \sum \rho_i \vec{u}_i h_i + \vec{q}_{rad} + \vec{u} \cdot (p\vec{\vec{I}} - \vec{\vec{\tau}})] = 0 \tag{2-3}$$

Vibrational energy conservation equations for different species are;

$$\frac{\partial \rho_i e_{iv}}{\partial t} + \nabla \cdot [\rho_i (\vec{u} + \vec{u}_i) e_{iv} + q_{iv})] = e_{iv} \frac{dw_i}{dt} + Q_{v,\Sigma} \tag{2-4}$$

Electronic energy conservation equation can be given as;

$$\frac{\partial \rho_i e_e}{\partial t} + \nabla \cdot [\rho_i (\vec{u} + \vec{u}_i) e_e + \vec{u} \cdot p_e \vec{\vec{I}} + q_e)] = e_e \frac{dw_i}{dt} + Q_{e,\Sigma} \tag{2-5}$$

where $Q_{v,\Sigma}$, and $Q_{e,\Sigma}$ are the net energy transfer between translational, vibrational, and electronic excitations. A key addition to the present formulation is that the rates of energy released from the vibrational-translational and electronic-translational interactions will be examined and modelled [5]. This subject shall remain as a sustained research focus into the future and will also be extended further to include ablation.

For calculating the equilibrated translational-rotational temperature and gas mixture density, the total internal energy is defined as

$$\rho e = \sum_{i \neq e} \rho_i (c_{v,i} T + \frac{\vec{u} \cdot \vec{u}}{2}) + \sum_{i \neq e} \rho_i e_{v,i} + \sum_{i \neq e} \rho_i \Delta h_i^o + \rho_e (c_{v,e} T_e + \frac{\vec{u}_e \cdot \vec{u}_e}{2}) \tag{2-6}$$

where Δh_i^o is the standard heat of formation. The vibrational energy of different species is obtained from the harmonic oscillator

$$e_{v,i} = \frac{R_u}{M_i} [\Theta_{v,i} / \exp(\frac{\Theta_{v,i}}{\kappa t} - 1)] \tag{2-7}$$

The pressure of the gas mixture is calculated with Dalton's law, including the contribution from the electrons collision

$$p = \sum \rho_i \frac{R_u}{M_i} T \tag{2-8}$$

where Θ_v is the characteristic vibrational temperature of species i, R_u is the universal gas constant, 8.314×10^7

erg/g-Mol K, and M_i is the molecular weight of chemical species i.

In the present formulation, a further breakdown of the internal energy in highly excited electron states is not included [2, 6, 7]. For the weakly ionized air the electrostatic force, $\rho_e E$, work done by this force on the control volume and Joule heating, $J \cdot E$, are not taken into consideration.

Kinetic Modelling For Internal Energy Transfer

The significance of relative time scales of the fluid dynamics and chemical kinetics can be easily demonstrated by the traditional demarcation for chemically reacting interactions as the equilibrium and nonequilibrium flows. The numerical results generated by a bench mark (GASP) for hypersonic flow are presented in the following three figures to illustrate the distinctive features of the flowfield involving chemical reaction. All these computational results are obtained in an axisymmetric frame with a dimension of (163x93) for a spherical cone (Ram-C-II). The flow conditions can be summarized by the Mach number of 27.09, Reynolds number of 1.38×10^4 based on the length of the model, and a static temperature of 198.6 K.

The energy distribution among different internal degrees of excitation, transport properties, and chemical composition of the gas can change substantially in the thin shock layer of the blunt body flowfield. The comparison of bow shock structures reveals a significant difference in the standoff distances of the two limiting conditions as it is presented in Figure 1. For the equilibrium limit, the decreased density ratio across the bow shock due to the instantaneously redistributed thermal energy to all internal degrees of freedom reduces the shock standoff distance to a value of 0.075 of the nose radius. From the computed temperature contours, the temperature of the gas mixture is also much lower than the more realistic nonequilibrium simulation.

The detailed comparison of the translational temperature distributions for perfect gas, nonequilibrium, and equilibrium conditions are depicted in Fig. 2. There is no need to describe the result of the perfect gas model but it is inserted in here as a frame of reference. The difference in the static temperatures is substantial; the peak temperatures of the nonequilibrium and the equilibrium computations are 20,787.46 K and 5,855.44 K respectively. In all the comparing results, the maximum temperature is consistently located immediately downstream of the shock. It can be easily anticipated that the conductive heat transfer rates at the stagnation region will be substantially different.

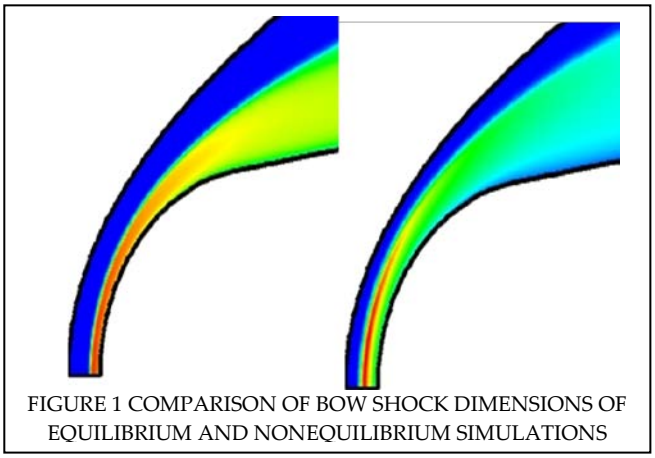

FIGURE 1 COMPARISON OF BOW SHOCK DIMENSIONS OF EQUILIBRIUM AND NONEQUILIBRIUM SIMULATIONS

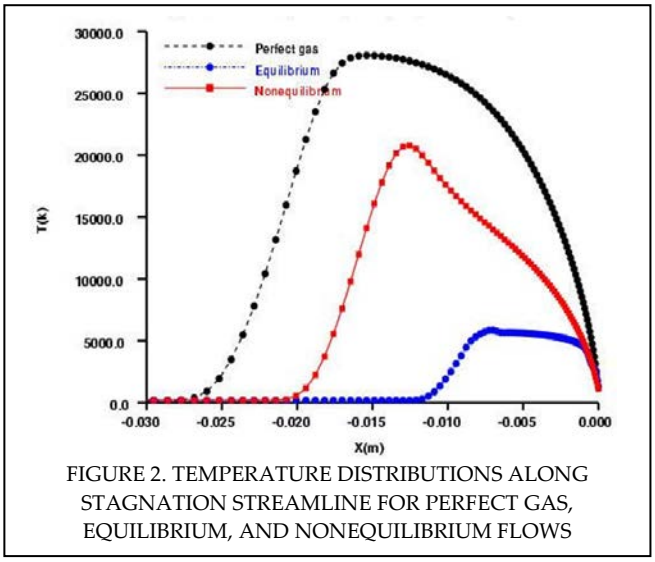

FIGURE 2. TEMPERATURE DISTRIBUTIONS ALONG STAGNATION STREAMLINE FOR PERFECT GAS, EQUILIBRIUM, AND NONEQUILIBRIUM FLOWS

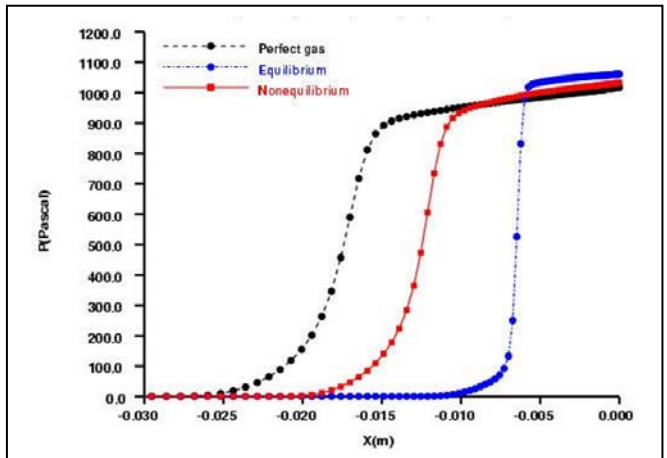

FIGURE 3. PRESSURE DISTRIBUTIONS ALONG THE STAGNATION STREAMLINE FOR PERFECT GAS, EQUILIBRIUM, AND NONEQUILIBRIUM FLOWS

Fig. 3 presents the comparison of the static pressure along the stagnation streamline for the same three cases studied. There is only a slight difference between results of the perfect gas and nonequilibrium model from the equilibrium condition on the body surface. This small difference is due to the existence of a larger fraction of free electrons for the equilibrium condition. Electronic excitation is also the only internal mode of the high-temperature gas that can contribute to the static pressure of the mixture. All other internal degrees of excitations are quantum phenomena that will not contribute to any net exchange of momentum with the ambient. In fact, the equilibrium computation generates the highest mass fraction of the free electrons which attains a value of $7.16\text{x}10^{-8}$ in comparison with the nonequilibrium limit.

The energy transfer among the internal degrees of freedom of high temperature air consists of two major mechanisms, energy exchange within the excited internal modes and the chemical kinetic processes. The chemical kinetic process can be further broke down into seven main mechanisms for energy transfer by Park [7]. They are ionization, electron impact dissociation, elastic collision between electrons and heavy particles, interaction between electrons and vibrational mode, energy exchange by the formation of species, associative ionization, and finally radiation losses. These processes are complex and our understanding of the physical chemical interaction in the molecular and atomic scales is extremely limited.

The chemical kinetic models of the present analysis are adopted based on some unique flow features immediately downstream of a strong shock. In this environment, the initial level of vibrational energy is far lower than that of the translational energy, and the energy exchange among the internal modes is dominated by the adjacent quantum level (ladder climbing). Especially, the vibrational quantum states are limited to the first few above the ground state. Therefore, the anharmonic correction may not be necessary. Most important, from the principle of detailed balance the classic result of Landau-Teller [8] becomes the backbone for the present kinetic modelling. The following kinetic models have guided the development of the practical applications [3-5,11-15].

The energy exchange between translational and vibrational modes is approximated by

$$Q_{TV} = \rho \frac{e_V^*(T) - e_V}{\tau_{TV}} e_V^*(T) = \frac{R\Theta_V}{e^{\Theta_V/T} - 1}, \quad e_V = \frac{R\Theta_V}{e^{\Theta_V/T_V} - 1} \qquad (3\text{-}1)$$

$$\tau = \frac{\kappa T^{1/2} Exp(\kappa / T)^{1/2}}{p[1 - Exp(-\Theta_v / T)]}$$

The energy transfer among the vibrational modes of different species has also been modelled by Master equation via a single quantum level. However, the relaxation time scale is provided by the experimental correlation of Millikan and White [9];

$$\tau_{TV} = 1.16 \times 10^{-3} \left(\frac{M_1 M_2}{M_1 + M_2}\right)^{1/2} \Theta_V^{4/3} [(T^{-1/3} - 0.15\left(\frac{M_1 M_2}{M_1 + M_2}\right) - 18.4 \qquad (3\text{-}2)$$

The preferential dissociation model by Treanor and Marrone [10] was adopted as the research progressed to the energy transfer between electronic and vibrational excitations;

$$Q_{ET} = \Sigma \varepsilon_{e,k} \left(\frac{dn_k}{dt}\right) \quad \kappa = Exp[(-(D - \nu E_i)/kT] \qquad (3\text{-}3)$$

The energy transfer between elastic electron-ion collisions is approximated by the formulation by Surzhikov et al [11].

$$Q_{Ei} = 1.21 \times 10^{20} x_e x_i \frac{T - T_e}{T_e^{3/2}} \ln \Lambda \qquad (3\text{-}4)$$

In this formulation, x_e and x_i denote the molar fractions of electron and positively charged ions, ln Λ is the Coulomb logarithm.

As a base for comparison, a global approximation for the energy transfer between heavy particle and electronic collisions formulated by Lee [12] has been used [13,14,15];

$$Q_{ET} = 3R\rho_e (T - T_e)\left(\frac{8RT_e}{\pi M_e}\right)^{1/2} \sum_{k \neq e} \frac{\rho_k N}{M_k^2} \sigma_{ek} \qquad (3\text{-}5)$$

A more recently developed on chemical-physical model that describes the electronic-vibrational kinetics can be found in the theory of Chernyi et al [16].

Transport Properties

A landmark of the kinetic theory of a diluted gas mixture is its ability in describing the transport properties of any gaseous mixture. To be consistent with the kinetic model of the internal structure of a gas; transport properties of the gas mixture for thermal diffusion, viscosity, and thermal conductivity are calculated from Boltzmann equation by using the Chapman-Enskog expansion [17];

Thermal diffusivity is;

$$D_{i,j} = 1.858\times10^{-3}\sqrt{T^3\frac{M_i+M_j}{M_iM_j}}/\sigma_{i,j}^2\Omega^{(1,1)} \quad (4\text{-}1)$$

The molecular viscosity is given as;

$$\mu = 2.67\times10^{-5}\sqrt{M_iT}/\sigma_i^2\Omega^{(2,2)} \quad (4\text{-}2)$$

and the thermal conductivities are

Mono-atomic gas;

$$\kappa_{i,m} = 1.989\times10^{-4}\sqrt{\frac{T}{M_i}}/\sigma_i^2\Omega^{(2,2)} \quad (4\text{-}3)$$

Poly-atomic gas;

$$\kappa_{i,p} = 2.519\times10^{-4}\sqrt{\frac{T}{M_i}}/\sigma_i^2\Omega^{(2,2)} \quad (4\text{-}4)$$

All collision integrals and cross sections are obtained from either the Lenard-Jones potential for non-polar molecules or a polarizability model for ion-neutral non-resonant collisions by Capitelli et al [18] and Levin et al [19].

The Chapman-Enskog theory gives the viscosity and thermal conductivity for a gas mixture, these formulas are also known as the Wilke's mixing rule [17];

$$\mu_{i,j} = \sum\frac{x_i\mu_i}{\sum x_i\phi_{i,j}} \quad (4\text{-}5)$$

$$\phi_{i,j} = \frac{1}{\sqrt{8}}(1+\frac{M_i}{M_j})^{-1/2}[1+(\frac{\mu_i}{\mu_j})^{1/2}(\frac{M_j}{M_i})^{1/4}]^2,$$

and

$$\kappa_{i,j} = \sum\frac{x_i\kappa_i}{\sum x_i\phi_i} \quad (4\text{-}6)$$

$$\phi_{i,j} = [1+(\frac{\kappa_i}{\kappa_j})(\frac{M_j}{M_i})^{1/4}]^2/[8(1+\frac{M_i}{M_j})]^{1/2}$$

The transport properties of the present analysis are derived from kinetic theory via the collision integrals and collision cross sections [18, 19]. For purpose of understanding, a very wide range of temperatures from 200 to 28,000 K for the eleven species of air mixture are calculated. According to the study of Capitelli et al [18], the calculated collision integrals are not dramatically dependent on the specific form of the potential models.

Figure 4 depicts the products of collision integral Ω(1,1) and its associated collision cross sections for all eleven species of air. The collision cross section is given in Angstrom squared (A^2) [18, 19]. The collision integral is a dimensionless double integral whose value is depended on the dynamics of binary collisions, thus is controlled by the intermolecular force law. From the calculated results, the magnitudes of the collision integral have the greatest value for the charged carried molecules, N2+, O2+, and NO+ over all other species in the high-temperature domain. Therefore the thermal diffusion of these species should have the lowest value. Meanwhile, the collision integrals of the polarized atomic species O+, N+, and the dissociated species N and O have a similar magnitude in the temperature regime calculated.

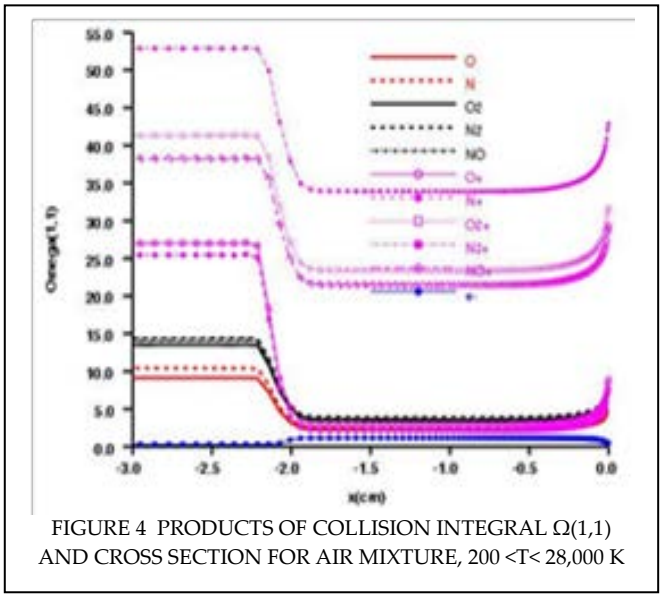

FIGURE 4 PRODUCTS OF COLLISION INTEGRAL Ω(1,1) AND CROSS SECTION FOR AIR MIXTURE, 200 <T< 28,000 K

The product of collision integrals Ω(2, 2) and its associated cross sections for calculating thermal conductivity and molecular viscosity of all air species in the investigated temperature domain are presented in Fig. 5. The variation of these products is less pronounced in the high temperature region to reflect a

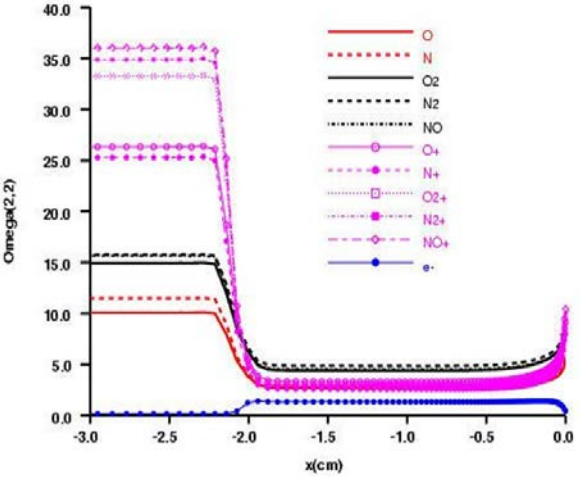

FIGURE 5PRODUCTS OF COLLISION INTEGRAL Ω (2,2) AND CROSS SECTION FOR AIR MIXTURE, 200 <T< 28,000 K

linear dependence to the local temperature and molecular weight of the species. Although there is substantial progress in the kinetic theory of gas for calculating transport properties, the specific comparison of the calculated transport properties still yields a difference of 16.3% to 24.2% in viscosity and thermal conductivity for high-temperature air using different sets of collision integrals in the temperature range from 300 to 30,000 K [19].

Chemical Kinetics

The high-temperature air mixture is considered to consist of 11 species; O, N, O2, N2, NO, O^+, N^+, $O2^+$, $N2^+$, NO^+ and e^-. For a non-equilibrium chemical reaction, the production rate of chemical species and heat release are calculated by the rate constants for the forward and reverse chemical reactions. The energy conversion in chemical reaction becomes an increasingly important process for energy transfer in hypersonic flows. However, based on the accumulated experience for hypersonic flow simulations, the chemical reactions and aerodynamics can still be loosely coupled to achieve the most efficient computation and this approach is adopted by the present study [3-5, 7, 20].

The rate constant is determined by the Arrhenius equation,

$$k_{f/r,i} = A_{f/r,i} T^{n_{f/r,i}} Exp[-\frac{E_{f/r,i}}{kT}] \qquad (5\text{-}1)$$

The forward reaction rate is frequently obtained from experimental observations and the reverse reaction rate can be determined by the Sharma approximation [3, 5, 7];

$$\frac{\kappa_{f,j}}{\kappa_{r,j}} \approx \kappa_e T_a \qquad (5\text{-}2)$$

The two most widely adopted non-equilibrium chemical reaction models are developed by Dunn and Kang [21] and Park [22]. Park's model is chosen simply because it has been frequently updated. In his model (48 elementary reactions are included) the reverse reaction rates are not provided. For the present analysis, the reverse reaction rate constants calculated by Surzhikov are used [5].

Several interesting features of nonequilibrium chemical reactions in the shock layer are easily illustrated by the heat release rate and the Damkohler number distribution generated by the GASP benchmark. Figure 6 gives the energy exchange rate

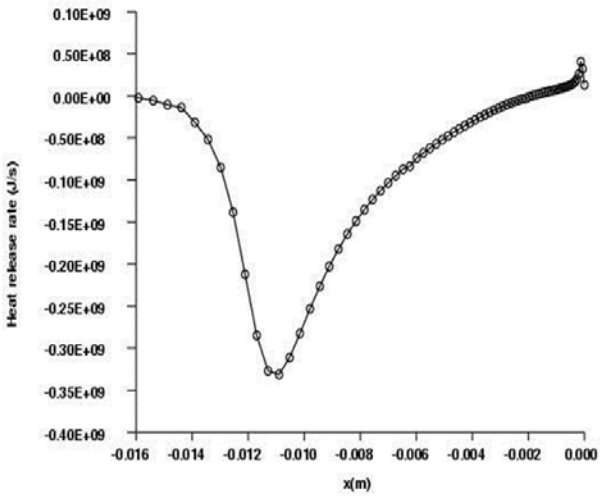

FIGURE 6 HEAT RELEASE RATE ALONG STAGNATION STREAMLINE

along the stagnation streamline to the surroundings. It is well known that in order to excite internal degrees of freedom of a gas mixture, an energy input is required to proceed. The behaviour of an endothermic reaction is clearly observed immediately downstream of the bow shock. However, when the gas mixture moves adjacent to the cooler blunt body then the chemical radicals begin to recombine; the local chemical reaction becomes exothermic. This fact leads to an important observation that the catalytic effect is an open issue for the chemically reacting flowfield around aerospace vehicles [3, 4, 7, 12, 15]. In the stagnation region, the chemical reactions and the chemical-physical processes are complex and are reflecting by the rapid rate of chemical reactions locally which demands additional attention to better

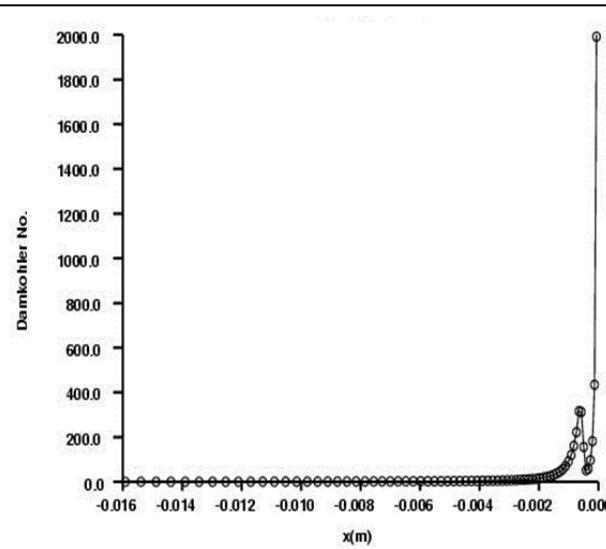

FIGURE 7 DAMKOHLER NUMBER DISTRIBUTION ALONG STAGNATION STREAMLINE

understand the energy exchange processes with a solid surface.

Figure 7 presents the calculated Damkohler number distribution along the stagnation streamline. In the major portion of the chemically reacting domain, the reaction rate is slightly faster or on the comparable order of the diffusion speed. However, the relative time scales drastically changes in the near-wall region, the Damkohler number shows multiple extremes. The maximum at the solid surface, in fact, exceeds a value of 2014. From the chemical reaction viewpoint, this behaviour can be interpreted as the mixing speed is much slower than the chemical reaction rate. Nevertheless, the most complex chemical reaction process is located near the fluid-solid interface rather than on the shock front. This result also points out the challenge in studying the ablation phenomenon.

Numerical process

The interdisciplinary partially differential equations (2-1) through (2-5) are solved by a combination of implicit, cell-centered finite-volume/finite-difference schemes; commonly adopted for solving the compressible Navier-Stokes equations [5,11,13-15]. The governing equations can be cast into the flux vector form;

$$\frac{\partial \vec{U}}{\partial t} + \nabla \cdot \vec{F} = \vec{R} \qquad (6\text{-}1)$$

where U is the dependent variables, $\vec{U} = \vec{U}(\rho, \rho\vec{u}, \rho e)$ and F is the flux vector component [23,24,25].

Although multiple numerical procedures were adopted as the solving scheme, the basic approach is the second-order implicit method [23, 24]. Especially, the NERAT [5, 23] uses three difference processes for solving the momentum, energy conservation, and the chemical species conservation equations. As a commonly accepted computational approach; the upwind-biasing approximation is applied to the convective and pressure terms, and central differencing is used for the diffusion and heat transfer terms. In addition, a flux-difference splitting procedure for shock capturing is implemented for solving the governing equations. The flux vectors at the control surface are written as the solution to the Roe-type approximate Riemann problem [25];

$$\begin{aligned}\delta U_i = {} & 1/2[F(U_L) + F(U_R)] - |M_{inv}|(U_R - U_L)]_{i+1/2} \\ & -1/2[F(U_L) + F(U_R)] - |M_{inv}|(U_R - U_L)]_{i-1/2}\end{aligned} \qquad (6\text{-}2)$$

where U_L and U_R are interpolated values of the dependent variables; ϱ, ϱ$\vec{u}$, and ϱe at the interface of the control volume and M_{inv} is the Jacobian matrix of the inviscid or convective terms [22,23].

A slope limiter is also used to control the discontinuous pressure jumps at the shock front. Time advancement is implicit to solve the flows that have a steady state asymptote. A min-mod limiter is adopted for some of the present computations;

$$\begin{aligned}(U_L)_{i+1/2} &= U_i + 1/4[(1-\kappa)\nabla U + (1+\kappa)\Delta U]_i \\ (U_L)_{i+1/2} &= U_{i+1} - 1/4[(1-\kappa)\Delta U + (1+\kappa)\nabla U]_{i+1}\end{aligned} \qquad (6\text{-}3)$$

where the one-side difference operators are; $\Delta U = U_{i+1} - U_i$ and $\nabla U = U_i - U_{i-1}$ respectively. The value of κ is assigned a value of -1 to yield the second-order fully-upwind differencing approximation.

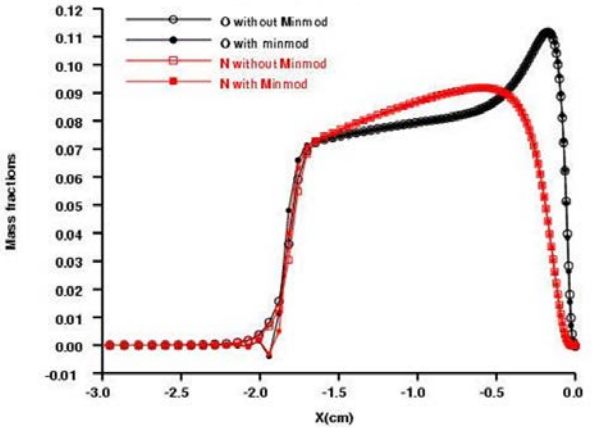

FIGURE 8 MASS FRACTION CALCULATIONS USING MIN-MOD LIMITER

The effectiveness of the slop limiter for controlling oscillations around the strong bow shock is revealed by the calculated species concentration for the chemical reactions. In one of the present solving schemes, the min-mod operator was applied to control the excessive numerical oscillation at the shock front. Figure 8 gives the mass fractions of atomic nitrogen and oxygen along the stagnation streamline. The slop limiter suppresses completely the numerical oscillations, but also increases the number of grid points required to capture the shock jump. This issue will be addressed again later in the discussion.

In order to concentrate on the rather complex physics, the numerical simulation is limited to an axisymmetric configuration. For the same reason, the important radiation-gas-dynamic interaction in hypersonic flow is also deferred from the present investigation but will be included in the continuing effort. Specifically radiation heat transfer will be treated by the multi-

group spectra approximation in which the radiating energy transfer is grouped according to the emitting frequencies [5, 23].

Numerical Results

Computational results of hypersonic flow over the Ram-C-II vehicle [26] are carried out. The basic configuration is a spherical cone with a nose radius of 15.24 cm and a semi-conical angle of 9 degree. The overall length of the vehicle is 129.54 cm. The flight test data were collected at altitudes from 53.3 to 85.3 km and at flight speed of 7.62 m/s with a small angle of attack. The flight test report consists of a detailed description of the data collection technique, flight trajectory information, and the data of the relatively rare ionized air concentration at a small angle of attack.

For now, two groups of computational simulations are limited to axisymmetric flow. The benchmark result from GASP is included together with the most recent results from NERAT [5, 11]. The latter represents the most recent and self-consistent kinetic model formulation for nonequilibrium hypersonic flow and is the key starting point of the present research.

For the purpose of providing a reference for understanding, the chemical composition, in mass fraction, along the stagnation streamline generated by the benchmark GASP is presented in Figure 9. The computation is obtained for a freestream Mach number of 27.09 with the freestream and wall temperatures of 198.6 and 1,000 K respectively. The body-oriented grid system (163×93) is also closely aligned with the shock envelope to facilitate shock capturing scheme by an analytical matching of spherical and hyperbolic functions. On this mesh system, the well-known "carbuncle" artefact near the axis of symmetry is completely absent which is frequently considered to be associated with the approximate Riemann formulation.

In this Figure molecular oxygen is nearly completely depleted and at the wall has a mass fraction of 8.17×10^{-4} which is the same order of magnitude as the charged species N+ and O+. The charged carried molecular components $N2^+$, $O2^+$, and the free electron e^- have the lowest mass fraction in the shock layer among all eleven species, and the former two species exhibit a strong dependence to the local temperature.

In the following, the simulated chemical compositions and the translational and vibrational temperatures from NERAT are presented. The numerical simulation is conducted at an altitude of 61 km with a freestream Mach number of 23.9 on a mesh system of (105×51). The freestream temperature according to the flight data is 244 K but the surface temperature is unknown. For most numerical simulations, this temperature has been prescribed in the range from 1000 to 1500 K and it is assumed that the surface is fully catalytic [13-15]. In the present investigation, the surface temperature is assigned a value from 300 to 1500 K extending the range of uncertainty. According to commonly accepted practices, the vibration temperatures are calculated from the model of harmonic oscillator [5,13-15]. The species concentration, however, will be given in terms of number density per unit volume to better describe the chemical composition. The numerical results will be validated by comparing with earlier simulations and available data [5, 13-15, 26]. Interpretation of new findings will be specially emphasized.

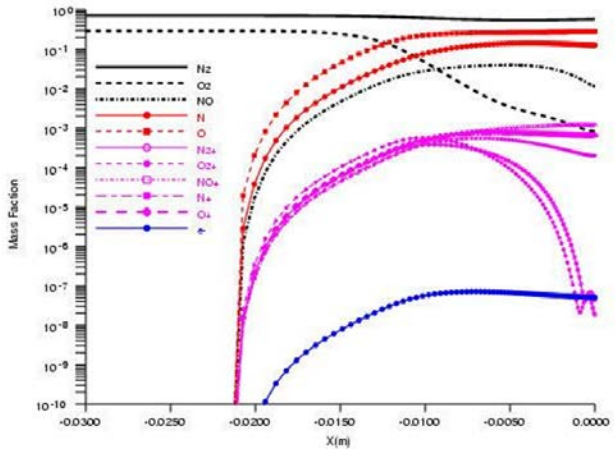

FIGURE 9 MACH NUMBER CONTOUR, M_∞=27.09, RE=1.385×104, T_∞ =198.6 K, (163×93) MESH

The calculated translational temperatures of the air mixture and the vibration temperatures of the molecular oxygen and nitrogen in the shock layer of RAM-CII along the stagnation streamline are given in Figure 10. For the lower surface temperature of 300 K, the peak translational temperature has a value of 14,754 K, the calculated vibrational temperature for molecular nitrogen and oxygen are 11,712 and 10,873 K respectively. These values are lower than the simulations using a much higher assumed surface temperature [13-15]. This discrepancy may be anticipated because at a lower surface temperature the increased heat transfer to the spherical cone significantly reduces the thermal energy in the shock layer. More importantly, this type of discrepancy has also been noticed from earlier simulations and has

even been pointed out by the fundamental research using *ab initio* approach [27]. Due to the lower translational temperature, the bow shock standoff distance is also shorter than other simulations; 0.09 cm versus 0.099 by Josyula et al [15] and 0.106 cm by Candler et al [13]. However the main feature of the temperature profiles remains in that, the energy is transfer from the translational mode to the vibrational mode and the temperatures of internal degrees of freedom are equilibrated at a short distance downstream of the bow shock.

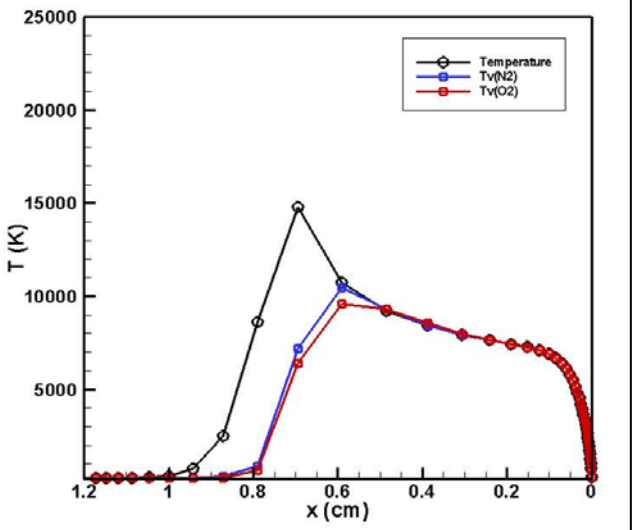

FIGURE 10 TEMPERATURES ALONG STAGNATION STREAMLINE, M_∞=23.9, T_∞=244 K, T_W=300K, (105X51) MESH

The corresponding chemical composition in number density per unit volume along the stagnation streamline is depicted in Figure 11. In this presentation, the particle number density is given in number per cubic centimetre, n/cm^3 or n/cc. In this graph the molecular oxygen under goes a wide range of variation from the freestream value of 1.12×10^{15}/cm^3 dips to a value less than 10^{13}/cm^3 in the shock layer and finally, due to recombination of atomic oxygen reaches a value higher than 1.1×10^{16}/cm^3 on the cone surface. The concentrations of O^+ and N^+ consistently have the lowest value less than 10^{13}/ cm^3 over the entire domain. The electron number density on the stagnation point has a value of 3.2×10^{13}/ cm^3. In the number density per unit volume format, the partially ionized, nonequilibrium air exhibits the classic behaviour of plasma; the flow medium is globally electrical neutral from the shock front until a thin sheath immediately adjacent to the surface. This behaviour fully justifies the omission of the electrostatic force from the present formulation.

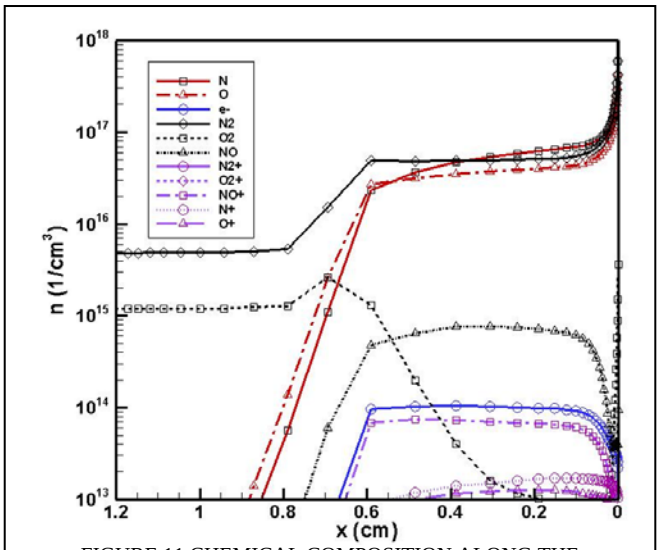

FIGURE 11 CHEMICAL COMPOSITION ALONG THE STAGNATION STREAMLINE, M_∞ =23.9, T_∞=244K, T_W=300K, (105□51)

In order to demonstrate the importance of grid topology for shock capture and highly clustered grid density near the solid surface, a redistribution grid system is implemented for the following computations. The rest of the simulations are performed on a coarser (55×41) mesh, but at an optimal distribution to focus on the kinetic modelling.

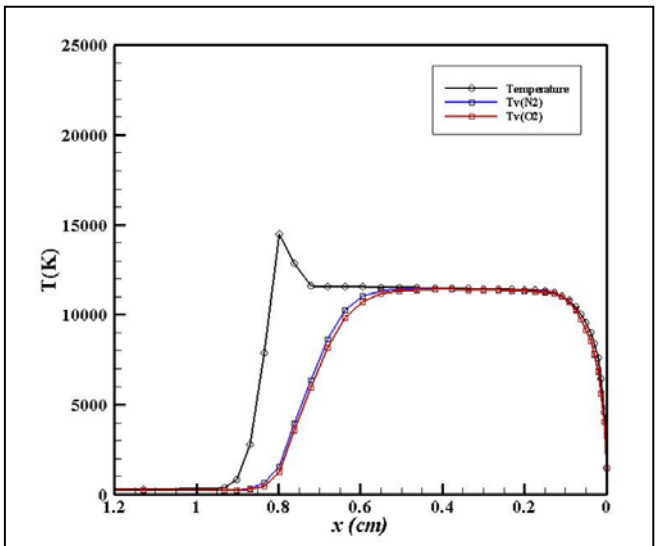

FIGURE 12 TEMPERATURES ALONG STAGNATION STREAMLINE,M_∞=23.9, T_∞=244 K, T_W=1500K, (55X41) MESH

Figure 12 depicts the translational and vibrational temperatures of molecular nitrogen and oxygen along the stagnation streamline with adjustment to the kinetic models. For the higher surface temperature of 1500 K, the peak translational temperature still has a value of 14,490 K, the calculated vibrational temperature for molecular nitrogen and oxygen are

11,411 and 11,396 K respectively. The calculated results display very small change from the results of the lower assumed surface temperature (300 K) and even a less effect due to the redistribution of grid points in the shock layer. For the present simulations using two different surface temperatures, the main feature of the temperature profile is unaltered in that the equilibrated temperature for vibrational, rotational, and translational modes has been reached at the distance of one-third of the shock-layer thickness downstream of the bow shock. This feature is shared by all numerical simulations [13-15] to reveal vibrational excitation requires a sufficient number of collisions to attain the same thermodynamic state as the translational and rotational modes. A minor difference in the result using the (55×41) mesh from the previous calculation is also observable; a nearly constant temperature region exists shortly after the equilibrated temperature of the internal modes is reached. Whether this feature is physically significant or not will be determined in future investigations.

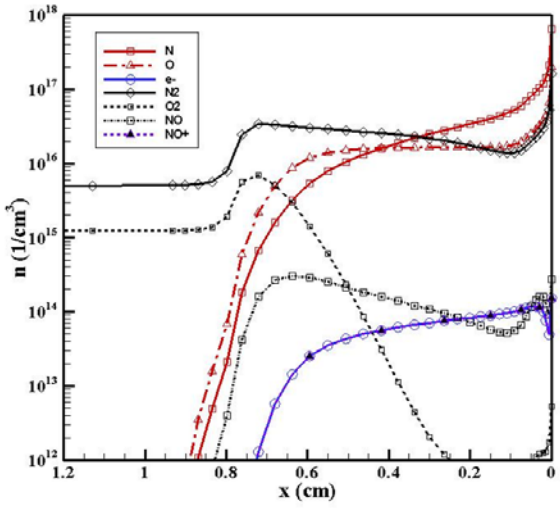

FIGURE 13 COMPOSITION ALONG STAGNATION STREAMLINE, M_∞=23.9, T_∞=244 K, T_W=1500K, (55×41) MESH

The corresponding species concentration along the stagnation streamline is depicted in Figure 13. In comparison with the previous calculation by the (105×51) mesh two significant differences stand out. First, the molecular components including the dissociated components N and O are nearly identical to the early simulation by an unrefined grid. The molecular oxygen still exhibits the most drastic change from the shock front to the stagnation point, but the recombined number density at the surface is much lower than the lower surface temperature calculation. A value of 5.3×10^{12}/cm^3 is noted at the stagnation point in contrast to a value of 1.1×10^{16}/cm^3. The second major difference is the concentrations of the charge carried atomic and molecular species O^+, N^+, $O2^+$, and $N2^+$ have now fallen below a value less than 10^{12}/cm^3. Therefore the number density of electrons is mostly balanced by the species NO^+ as it is expected to behave as the globally neutral partially ionized plasma.

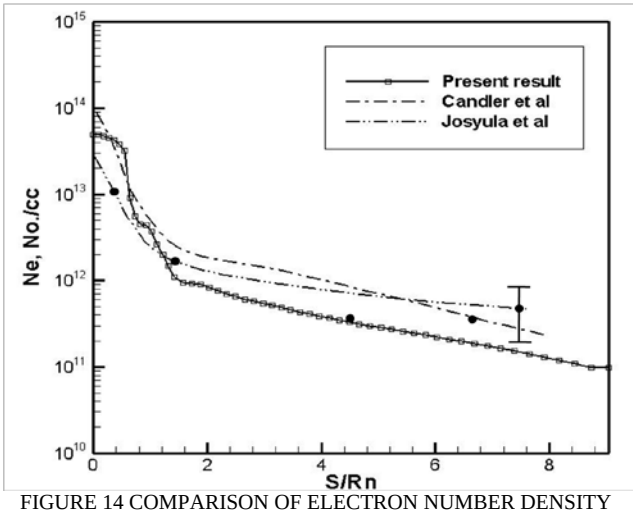

FIGURE 14 COMPARISON OF ELECTRON NUMBER DENSITY DISTRIBUTION ALONG RAM-CII WITH DATA

The only validation of the present results is derived from the comparison of electron number densities with the flight data by Jones and Cross [26]. The major portion of their electron number density data is measured by a reflectometer and a checking point by an electrostatic probe at the distance around 8 nose radii from the stagnation point. The data by the reflectometer represents the averaged peak value at the sample location and the probe data is the time-averaged value among the innermost and the outermost probes. The estimated error bar of the probe data covers a range of the peak-to-peak density fluctuation from 3.0×10^{11}/cm^3 to 1.2×10^{12}/cm^3 due the body motion. The comparison of the present computational result with flight data is depicted in Figure 14. In spite of a noticeable difference in the predicted temperature profiles in the shock layer by the present study from other computational simulations [13-15], the agreement with the flight data is reasonable and is comparable with earlier numerical results by Candler et al [13], Josyula et al [14].

However, a better understanding of the quantum energy transition among internal degrees of excitation of a high-temperature gas can only be achieved through an *ab-initio* approach of the computational chemical-physics. This computational simulation is based on the first principle of the collision process

from classic mechanics, and requires knowledge of inter-atomic forces exerted by the potential energy. The computational resource requirement of this approach is extremely intensive. At the present, this research is limited to simulation of a single gas species [27].

Conclusion

An internally consistent formulation for simulating the hypersonic nonequilibrium flow based on the kinetic theory of gas has been initiated. The present investigation combines the physically based kinetic models for internal degrees of freedom and the most recent advance in collision integrals research for transport properties of high-temperature air.

Different implicit algorithms are adopted to solve separately the conservation equations for species concentration, vibrational, electron energy equation, and finally coupled with the compressible interdisciplinary equations. The solving scheme has been proven to be computational stable and accurate in comparison with parallel efforts.

The present progress built on the luminary pioneering efforts in chemical-kinetic models reveals just the first step in developing an accurate modelling and simulating tool for nonequilibrium hypersonic flow simulations. The high fidelity descriptions of the complex quantum chemical-physical phenomena for better understanding still requires a combined and sustained effort by *ab-initio* computations and non-intrusive experimental observations for analysing ablation including the pyrolysis and radiation phenomena.

ACKNOWLEDGMENT

The authors are sincerely appreciated the sponsorship by Dr. J. Schmisseur and Dr. F. Frahoo of the Air Force Office of Scientific Research, Air Force Research Laboratory.

REFERENCES

[1] Chapman, S. and Cowling, T.G., The Mathematical theory of non-uniform Gases, Cambridge University Press, 1964, pp134-150.

[2] Clarke, J.F. and McChesney, M., The Dynamics of Real Gases, Butterworth Inc., Washington D.C., 1964, pp. 66-86.

[3] Park, C., Chemical-kinetic Parameters of Hypersonic Earth Entry, J. of Thermophysics and heat Transfer, Vol. 15, No. 1, 2001, pp.76-90.

[4] Chen, Y.K. and Milo, F.S., Navier-Stokes Solutions with Finite Rate Ablation for Planetary Mission Earth Mission Earth Reentries, J. Spacecraft and Rockets, Vol. 42 No. 6, 2005, pp.961-970.

[5] Surzhikov, S.T. and Shang, J.S., Kinetics Models Analysis for Super-Orbital Aerophysics, AIAA 2008-1278, Reno NV, 2008.

[6] Zel'dovich, Ya. B. and Yu. P. Raizer, Physics of Shock Waves and High-temperature Hydrodynamic Phenomena, Dover Publications, Inc., Mineola, NY, 2002, pp. 177-232.

[7] Park, C., Nonequilibrium Hypersonic aerodynamics, John Wiley & Sons, New York, NY, 1989, pp.89-118.

[8] Landau, L. and Teller, E., Zur Theore der Schalldispersion, Physik Z. Sowjetunion, b. 10, h. 1, 1936, p.34.

[9] Millikan, R.C., and White, D.R., Systematics of vibrational Relaxation, J. Chemical Physics, Vol. 39, No. 12, 1963, pp.3209-3213.

[10] Treanor, C.E. and Marrone, P.V., Effect of Dissociation on the rate of Vibrational Relaxation, Physics of Fluids, Vol.5, No. 9., 1962, pp.1022-1026.

[11] Surzhikov, S., Sharikov, I, Capitelli, M., Colonna, G, Kinetic Models of nonequilibrium Radiation of Strong Air Shock Waves, AIAA 2006-0586, Reno NV 2006.

[12] Lee, J.H., Basic Governing Equations for the Flight Regime of Aeroassisted Orbital Transfer Vehicles, Progress in Aeronautics and Astronautics: Thermal Design of Aeroassisted Orbital Transfer Vehicles, Vol. 96, AIAA, New York, NY, 1985, pp.3-53.

[13] Graham, G.V., and MacCormack, R.W., Computation of Weakly ionized Hypersonic Flows in Thermochemical Nonequilibrium, J. Thermophysics, Vol. 5, No. 3, 1991, pp. 266-272.

[14] Scalabrin, L.C. and Boyd, I.D., Numerical Simulation of Weakly Ionized Hypersonic Flow of Reentry Configurations, AIAA 2006-3773, San Francisco, June 2006.

[15] Josyula, E. and Bailey, W.F., Governing Equations for Weakly ionized Plasma Flow field of Aerospace Vehicles, J. Spacecraft and Rockets, Vol. 40, No. 6, 2003,

pp. 845-857.

[16] Chernyi, G.G., Losev, S.A., Macheret, S.O., Potapkin, B.V. Physical and chemical processes in Gas Dynamics: Physical and chemical kinetics and thermodynamics of gases and plasmas. Vol. 2. Progress in Astronautics and Aeronautics, Ed. P. Zarchan, Vol. 197, 2004.

[17] Bird, R.B., Stewart, W.E., and Lightfoot, E.N., Transport phenomenon, 2nd edition, John Wiley & Sons, New York, 2002, pp. 25, 274, 526.

[18] Capitelli, M., Gorse, C., and Longo, S., J. ,Collision Integrals of High-temperature Air Species, Thermophysics and Heat Transfer, Vol. 14 No. 2, 2000, pp259-268.

[19] Levin, E. and Wright, M.J., Collision Integrals for Ion-Neutral interactions of Nitrogen and Oxygen, J. Thermophysics and Heat Transfer, Vol.18 No 1, 2004, pp.143-147.

[20] Shang, J.S., Numerical Simulation of Hypersonic Flows, Computational Methods in Hypersonic Aerodynamics, Computational Mechanics Publications, South Hampton UK, 1992.

[21] Dunn, M.G. and Kang, S.W., Theoretical and experimental Studies of reentry Plasma, NSA CR 2232, April 1973.

[22] Park, C., Review of Chemical Kinetics Problems of Future NASA Missions, I Earth Entries, J. Thermophysics and Heat Transfer, Vol. 7 No. 3 1993.

[23] Surzhikov S.T. TC3: Convective and Radiative Heating of MSRO for Simplest Kinetic Models. Proceedings of the International Workshop on Radiation of High Temperature Gases in Atmospheric Entry. Part II.30 Sept.-1 Oct., 2005. Porquerolles France. (ESA SP-583, May 2005, pp.55-62)

[24] Rumsey, C., Sanetrik, M., Biedron, R., Melson, N.D., and Parlette, E, Efficiency and Accuracy of Time-Accurate Turbulent Navier-Stokes Computations, Computer & Fluids, Vol. 25, No. 2, 1996, pp.217-236.

[25] Roe, P., Approximate Riemann Solvers, Parameter Vectors, and Difference Scheme, J. Computational Physics, Vol. 48, 1981, pp.357-372.

[26] Jones, L.J. and Cross, A.E., Electrostatic Probe Measurements of Plasma Parameters for Two Reentry Flight Experiments at 25,000 feet per second, NASA TN D 66-17, 1972.

[27] Chaban, G., Jaffe, R., Schwenke, D.W., and Huo, W., Dissociation Cross Sections and Rate Coefficients for Nitrogen from Accurate Theoretical Calculations, AIAA 2008-1209, Neo, NV, Jan. 2008.